

This is the peer reviewed version of the following article: "Loss analysis in perovskite photovoltaic modules", which has been published in final form at DOI <https://doi.org/10.1002/solr.201900338>

This article may be used for non-commercial purposes in accordance with Wiley Terms and Conditions for Use of Self-Archived Versions.

Loss analysis in perovskite photovoltaic modules[†]

*Lucija Rakocevic**, *Laura E. Mundt*, *Robert Gehlhaar*, *Tamara Merckx*, *Tom Aernouts*, *Martin C. Schubert*,
Stefan W. Glunz, *Jef Poortmans*

Lucija Rakocevic, Dr Robert Gehlhaar, Dr Tamara Merckx, Dr Tom Aernouts, Prof. Jef Poortmans
imec, Kapeldreef 75, 3001 Leuven, Belgium

lucija.rakocevic@imec.be

Lucija Rakocevic, Prof. Dr Jef Poortmans

Departement Elektrotechniek - ESAT, KU Leuven, 3001 Leuven, Belgium

Dr Laura E. Mundt, Dr Martin C. Schubert, Prof. Stefan W. Glunz

Fraunhofer Institute for Solar Energy Systems, 79110 Freiburg, Germany

Prof. Stefan W. Glunz

University of Freiburg, Laboratory for Photovoltaic Energy Conversion, 79110 Freiburg, Germany

Prof. Dr Jef Poortmans

University of Hasselt, 3590 Diepenbeek, Belgium

Keywords: perovskite thin film photovoltaic modules, loss characterization, luminescence, thermography

DOI: 10.1002/

Article type: Full Paper

Abstract

Hybrid metal halide perovskite-based thin-film photovoltaics have the potential to become the next generation of commercialized PV technology with certified power conversion efficiencies reaching 24 %

on 0.1 cm² area devices. Recent efforts in upscaling of this technology resulted in an efficiency of 12.6 % for 354 cm² modules. Still, upscaling loss for perovskite-based photovoltaics is higher than for any other PV technology. In this study, we investigate these upscaling losses, with a focus on layer inhomogeneities, for devices with aperture area of 0.1, 4 and 100 cm². With use of electro-luminescence, dark lock-in thermography, micro photoluminescence spectroscopy and electron spectroscopy we analyze and group layer inhomogeneities with minimal size of 10 μm and compare loss mechanisms for radial and linear deposition techniques. Analysis leads us to defining processing pitfalls, where understanding and control of perovskite crystal formation plays the crucial role.

Perovskite-based thin-film photovoltaic (TFPV) technology has taken the place of the most promising research technology to enter the photovoltaics market in the near future. This happened due to the remarkable semiconductor characteristics of hybrid metal halide perovskites, including the adjustable band gap with a high absorption coefficient, high charge carrier mobility for an organic based material, high ratio of diffusion length to absorber thickness and high tolerance to defects.^[1;2;3;4] Due to its low formation energy, perovskite semiconductors have been successfully processed using various processing techniques including vapor deposition and low-temperature solution-based techniques, such as spin coating, ink-jet printing, spray coating, soft cover deposition, blade coating and slot die coating.^[4;5;6;7;8;9] In addition to the low-energy processing routes, the commonly used materials are abundantly available and allow for a low-cost fabrication in comparison to existing commercially available PV technologies.^[2;10] However, in order to achieve successful commercialization, perovskite TFPV research has to give answers to long term stability of large-area devices with high power conversion efficiency.

The complexity of the perovskite polycrystalline structure and the multi component crystalline lattice makes the stability of perovskite TFPV highly dependent not only on the processing conditions and characteristics of the perovskite layer but also on the choice of transport and contact layers.^[3] Strategies focused on altering perovskite composition and optimizing the device structure have shown promising results towards 1000 hour stability on small-area devices.^[3;11]

One key challenge has been the increase of the active cell area from few square millimeters to full wafer size while maintaining efficiency and reproducibility. Increase in research activity focused on upscaling perovskite devices has resulted in efficiencies of 12.6 % for 354 cm² active area device.^[12] This is related to gaining insight into the perovskite crystallization process.^[4;12;13;14;15;16;17;18] Although factors such as precursor and solvent interaction, process atmosphere, temperature, precursor and substrate interaction, as well as the deposition technique itself were identified to have crucial impact on the device efficiency, further un-

derstanding of the influence of these factors is necessary in order to control perovskite crystallization and achieve reliable and reproducible thin film layers.^[1;2;4;19;20] Despite advances in performance of larger area devices, efficiency decrease with device area increase is still significantly higher for perovskite TFPV than for other technologies with similar lab scale efficiencies (Si, CdTe, CIGS).^[2;20;21;22;23] Currently, the efficiency loss from the best reported sub 1 cm^2 perovskite cell^[24] to 354 cm^2 module^[12] amounts to $\sim 50\%_{rel}$. Therefore, further understanding of loss mechanisms is needed to reach efficient large-area devices.

Upscaling perovskite devices has taken two routes: large-area cells and large-area modules with monolithic serially interconnected cells. The increase in cell area in both cases faces efficiency loss due to the sheet resistance of the contact layers^[25;26] and inhomogeneities in layers of the perovskite device stack^[4]. Moreover, the upscaling to module devices introduces additional losses due to cell to cell interconnections, in the form of an inactive area loss and an interconnection resistance loss.^[27;28;29;30;31] The sheet resistance loss, inactive area loss and interconnection resistance loss can be minimized with cell or module design and optimization of interconnection patterning process. Once minimized, these losses stay constant with scaling. On the other hand, perovskite materials and devices are prone to lateral heterogeneities ranging from inter-grain microscopic non-uniformity^[32;33;34;35] to macroscopic, process-related inhomogeneities^[36], making layer inhomogeneity loss the obstacle to highly efficient large area devices. The effect of the layer inhomogeneity loss on the efficiency of perovskite modules when increasing the aperture area is seen in Figure 1a, where SPICE based simulation[†] is used to define the share of sheet resistance, inactive area and interconnection resistance losses in total cell to module upscaling loss. Minimizing the layer inhomogeneity loss requires identifying inhomogeneity types and their origin.

Thermography and luminescence based imaging techniques are well-established and in-line compatible characterization techniques, widely applied in commercialized PV technologies among solar cell production lines and module manufactures. In perovskite based PV, there are multiple studies where photoluminescence (PL) mapping has been used to analyze heterogeneity in perovskite films on grain size scales, including band-gap variations, charge carrier dynamics, stability etc..^[37;38;39] Recently, Mundt et al. demonstrated a spatially resolved analysis of efficiency loss in PSCs based on dark lock-in thermography (DLIT) and multi-wavelength LBIC. Local layer inhomogeneities were revealed to be the major loss contribution in cells with an active area of 1.1 cm^2 .^[36]

Taking into account existing knowledge and peculiarities^[40] of imaging perovskite PV devices, in this study we apply electroluminescence (EL), DLIT and microscopic photoluminescence spectroscopy (μ PLS) tech-

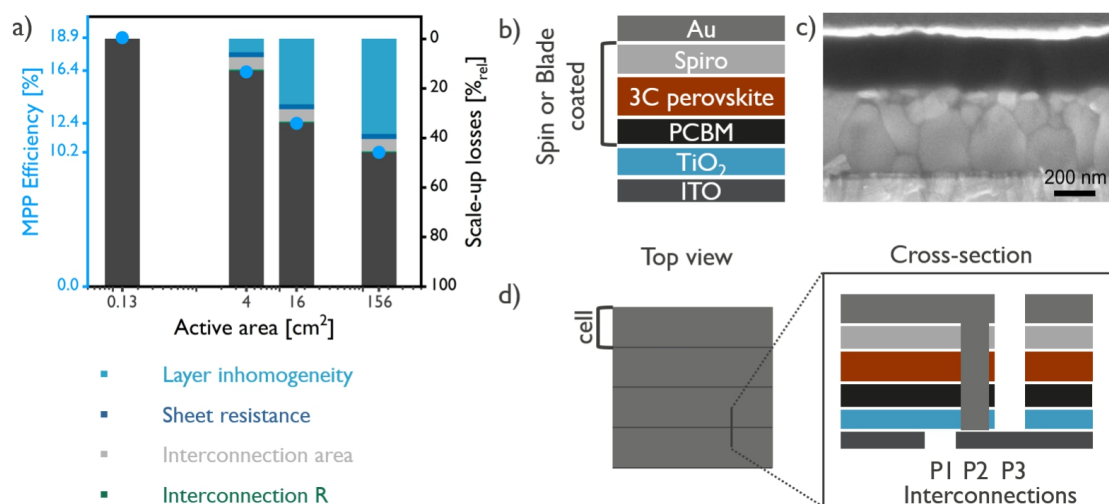


Figure 1: a) Losses in perovskite samples upscaling from 0.13 cm² cell to, 4, 16 or 156 cm² modules. The different colors represent each of the upscaling losses: inhomogeneity loss, sheet resistance loss, interconnection inactive area loss and interconnection resistance loss. b) Scheme of perovskite planar nip architecture used in this study. c) SEM image of the cross section with nip stack layers visible. d) Design of the 4 cm² module with monolithic serially interconnected cells and the cross section indicating interconnection patterns.

niques to identify and classify layer inhomogeneities and electron microscopy to define causes of inhomogeneity loss in perovskite PV modules. Moreover, since spin coating, as a radial deposition method, is the most commonly used method for processing lab-scale perovskite devices, we show the difference in inhomogeneity losses going from radial to linear deposition for planar nip architecture on 4 cm² modules and effects on 100 cm² modules. Based on this analysis, crucial processing steps and conditions that can improve large area device performance are identified.

1 Methods

Perovskite devices used in this study are planar nip architecture with three types of devices: 0.1 cm² cells; 4 cm² modules and 100 cm² modules. Small area cells and 4 cm² modules have been processed on 9 cm² substrates using spin coating (radial deposition) or blade coating (linear deposition) of perovskite and transport layers (Figure 1b), while 100 cm² modules are processed only by blade coating. Prior to stack processing, substrates are cleaned using a cleaning cycle of soap in DI water-DI water-acetone-isopropyl alcohol in ultrasonic bath at 55 °C. Back and front electrodes are evaporated and sputtered, respectively. The studied nip stack consists of indium thin oxide (ITO)/titanium oxide/PCBM/Cs_{0.05}(MA_{0.17}FA_{0.83})_{0.95}Pb(I_{0.84}Br_{0.16})₃/Spiro OMeTAD/gold, as shown in Figure 1. Substrates with deposited ITO are purchased

from Colorado Concept Coatings LLT. Compact e-beam deposited 20 nm of TiO_2 ^[7] is used as electron transport layer, ETL. Solution processed phenyl-C60-butyric acid methyl ester (PCBM) dissolved in chlorobenzene (20 mg/ml) is used to passivate the interface.^[41] We employ a three cation perovskite (CsFAMAPbIBr) due to its improved performance.^[42] Finally, Spiro-OMeTAD dissolved in chlorobenzene (80 mg/ml), doped with 28.5 $\mu\text{l/ml}$ of 4-tert-butylpyridine (TBP) and 17.5 $\mu\text{l/ml}$ of bis(trifluoromethane) sulfonamide lithium salt (Li-TFSI, 520 mg/ml in acetonitrile) serves as hole transport layer (HTL) with thermally evaporated 80 nm of gold as back electrode. Transfer of the spin coating recipe to blade coating is achieved by changing the solvent system of the perovskite layer from DMF/DMSO to DMF/NMP. The crystallization of the blade coated perovskite is improved by introducing gas quenching to form an intermediate phase before perovskite crystallization through heat treatment.^[4;14] Complete stack is processed in nitrogen atmosphere except for 12 hrs of oxygen doping after Spiro-OMeTAD deposition. Interconnection of cells in the module (4 cells in 4 cm^2 and 20 in 100 cm^2 module) is accomplished using laser patterned P1 and mechanically patterned P2 and P3 described in previous publication (Figure 1d and Figure S1).^[31]

Processed 4 cm^2 modules are encapsulated using glass to glass edge sealing^[39], in order to avoid degradation due to air and humidity exposure. To assure no damage has been caused, samples are remeasured after encapsulation using the method described here. All imaging characterization techniques in this study were performed on encapsulated samples, unless otherwise specified.

The current-voltage characteristics for cells and modules are measured in nitrogen atmosphere, employing a class A Abet Sun 2000 solar simulator generating an AM1.5G spectrum. The light source of the solar simulator is calibrated using a Fraunhofer ISE certified silicon reference cell with KG3 filter. The measurement procedure consists of a J-V hysteresis sweep and maximum power point tracking (MPPT). The J-V hysteresis sweep is a J-V sweep where voltage is swept from open circuit (OC) to short circuit (SC) back to OC condition at a scan rate of 1 V/s for cells and 4 V/s for modules with a measurement delay of 10 ms. MPPT is performed using the Tracking algorithm^[43] with a measurement time of 180 s, a measurement delay of 100 ms and voltage steps of 10 mV for cells and 50 mV for module devices. In all cases, MPPT stabilized at efficiency values comparable to values from a reverse (OC-SC) J-V scan.

EL images are captured using a Princeton Instruments PIXIS 1024 camera, model 7520 with Nikon macro lens. Acquisition time is varied from 0.1 to 1 s. All images have been normalized to 1 s. Constant voltage of 4.5 or 5 V is applied to the sample for a period of maximum 30 minutes, while the output current is recorded each second. Full device EL images are acquired every minute in the first five minutes, after

which the images are acquired every five minutes. The samples are kept in dark and have no light or voltage preconditioning prior to any of the presented measurements.

DLIT measurements are performed on encapsulated devices placed on a temperature-controlled chuck at 25 °C at a lock-in frequency of 30 Hz with bias voltage of at least 300 mV higher than the V_{OC} determined by J-V sweep measurements of each device.

Micro photoluminescence spectroscopy (μ PLS) mapping is performed on completed and encapsulated samples. A confocal microscopy setup with movable XY stage is used, scanning the sample while collecting the entire PL emission spectrum at every point.^[44] Excitation is achieved via a diode laser at a wavelength of 635 nm in continuous wave mode at an intensity of 6 to 600 mW/cm² for an excitation spot size of approximately 200 to 2 μ m FWHM for full module or local area map respectively. The emitted PL is collected by the same lens before being collimated onto a pinhole, excluding emitted light outside the focal plane. Spectrally resolved via a 600 grooves/mm grating spectrometer, the signal is detected using a silicon line charge-coupled device (CCD). Maps of the full module area were obtained with 200 μ m resolution to detect and localize inhomogeneities. Local maps were obtained with higher resolution (10 μ m) in order to identify the nature of detected inhomogeneities. Aside from full module and local maps, spot measurements consist of illuminating a spot of a radius of 200 μ m and measuring the temporal evolution of PL signal from the illuminated area for a period of 20 minutes. A Gaussian curve was fitted to the PL spectra, based on which maps of peak position and peak width are acquired.

Consequential to the imaging characterization, localized inhomogeneities were analyzed using a Zeiss Dual Beam Workstation Auriga 60 for scanning electron microscopy (SEM) and focused ion beam (FIB) imaging. Moreover, in order to understand the origin of some of the frequently occurring inhomogeneities, aside from FIB cross sectional analyses, an energy dispersive X-ray spectroscopy (EDX) Bruker Quantax 400 with single shot detector is used for spot and mapping analyses. For the micro characterization of the specific inhomogeneities, the device encapsulation is removed. Images are acquired with all layers, or with gold layer removed to better examine chemical structure of specific areas. Images are acquired using voltages of 5-7 kV and currents up to 500 pA, while for EDX spot analysis voltages up to 15 kV are used.

The full characterization procedure consists of five steps, as shown in Figure S2. The first step is a performance analysis using J-V and MPPT measurements. The modules are imaged using EL and DLIT in steps 2 and 3, in order to examine device uniformity and to localize problem areas. In step 4 the full module area and local mm sized areas are mapped using μ PLS. Finally, the module encapsulation is removed in order to

examine inhomogeneities using SEM, EDX and FIB (step 5 Figure S2).

2 Results and Discussion

Perovskite modules are investigated for layer inhomogeneities using the described five step characterization procedure. Two of the five steps in the process are based on perovskite luminescence images, where due to temporal changes in device luminescence^[37;39;40;45;46;47], we used the same measurement method for all analyzed samples[†]. The characterization procedure was employed to detect and analyze inhomogeneities with the highest resolution of 10 μm . The detected inhomogeneities are classified into five types. The types are defined based on inhomogeneity size and the characterization method used to localize them, as shown in Figure 2. The aim of the classification is to indicate which characterization method can be used to localize specific macroscopic process-related inhomogeneity. A summary of the classification is given in Table 1 identifying the source and the effect of each type of layer inhomogeneity on module performance. Moreover, we propose strategies that can be used in current module processing to avoid identified inhomogeneity types. Following is the detailed analysis of each inhomogeneity type. Subsequently, we compare upscaling losses in spin and blade coated modules identifying difference in upscaling losses, specifically layer inhomogeneities between the two deposition methods.

2.1 Inhomogeneity classification

2.1.1 Type 1

Type 1 inhomogeneities are detected using forward bias DLIT as hot spots in the active area of the cell and can be locally mapped with high resolution μPLS , as shown in Figure 3. The size of these inhomogeneities can be 30 μm or less. In the example shown in Figure 3, we find that a type 1 inhomogeneity is formed in the spin coated module around a micrometer sized organic (C-based) particle which disrupts perovskite formation to create a feature which is not easily covered by HTL. Such inhomogeneities can be a shunt in the cell, allowing the local current flow between metal and conductive oxide electrodes. Since these inhomogeneities are mainly observed where perovskite layer is interrupted, we postulate that they originate partially from unfiltered transport layer solutions, PCBM in this case, and partially from the lack of cleanliness of pre-perovskite layer processing steps.

Further DLIT characterization of type 1 inhomogeneities to define which inhomogeneities are shunts would

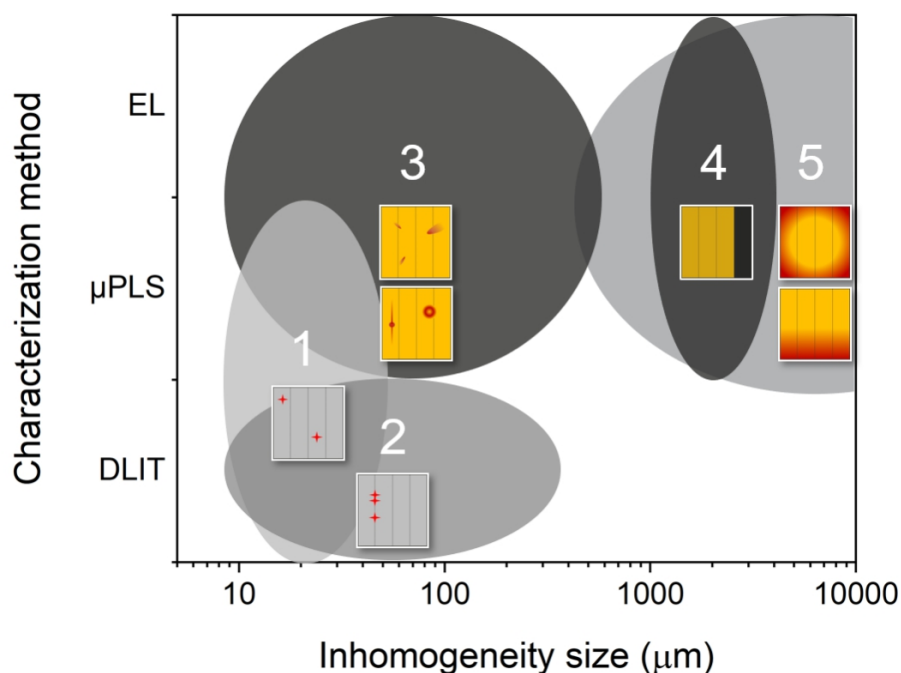


Figure 2: Grouping of inhomogeneities into five types depending on their size and imaging method used to detect them.

involve imaging a perovskite sample during reverse bias. This measurement was not attempted with studied samples due to possible device failure.^[48] However, for 50% of the blade coated modules that had type 1 inhomogeneities, the existence of this inhomogeneity was detrimental to the short term performance of the cell, which indicates shunt-like impact of the inhomogeneity on the affected cell. Moreover, in cases where dark I-V measurements are available one can quantify power loss due to each of the type 1 inhomogeneities, as previously demonstrated.^[36]

2.1.2 Type 2

Type 2 inhomogeneities are located at the interconnection of cells in a module and span between 10 to 300 μm in size. They can be identified using DLIT, but are difficult to image using other methods from this study. High resolution LBIC imaging would be optimal for imaging these inhomogeneities.^[49;50] Interconnections of cells in a module consist of three patterning steps as shown in Figure 1d, where P1 and P3 represent disconnection/isolation of front or back contact respectively and P2 a contact between front and back electrode of neighboring cells. Isolation of P1 or P3 can be interrupted by a conductive particle or redeposition of material after removal^[51;52], respectively as shown in Figure 4d. In these cases the type 2 inhomogeneity can compromise P1 or P3 isolating properties and result in cell exclusion from module circuit. For samples

2.1 Inhomogeneity classification

Table 1: The classification of identified inhomogeneities into five types.

	Type 1	Type 2	Type 3	Type 4	Type 5
Characterization method	DLIT and local maps μ PLS	DLIT	EL and μ PLS	EL and μ PLS	EL and μ PLS
Size	30 μ m or less	up to 300 μ m	up to 500 μ m	full cell	mm sized areas
Source	Unfiltered PC ₆₀ BM solution and lack of process cleanliness	Conductive particles in P1 or P3 compromising isolation	Non-optimized colloidal precursor solution and process cleanliness	Presumed to be due to interconnection defects	Differences in non-radiative recombination due to perovskite /PCBM/TiO ₂ interface
Effect on performance	Can cause full cell damage during short term performance	Decrease in FF or inactive cells due to dysfunctional interconnections	Decrease in J_{SC} and V_{OC} performance and possible effect on long term stability	Inactive cells causing lower V_{OC} in modules	Lower J_{SC} due to current mismatch among cells in a module
Loss decrease strategy	Filter solutions and assure controlled process atmosphere for all steps	Laser patterning with particle suction system	Precursor solution engineering and optimization of deposition method for controlled crystallization	Optimized patterning method using laser ablation	Optimize deposition method (precursor deposition, solvent evaporation, drying) for perovskite homogeneity

analyzed in this study, P2 and P3 interconnections are formed using mechanical patterning, where due to material accumulation formation of larger particles in P3 is more common (Figure 4c). To decrease this possibility, laser patterning with gas flow or particle suction system is used as a material removal method.

2.1.3 Type 3

Type 3 inhomogeneities range up to 500 μ m in size with greater effect on formed perovskite layer, which makes them easily visible to the naked eye. In spin coated samples, these inhomogeneities can create comet like structures in the thin perovskite or transport layers (Figure 5), while in blade coated samples they cause stripe shaped lines of thinner layers in the coating direction or concentric rings features around them (Figure 6). These inhomogeneities are easily visible in EL images and μ PLS maps due to differences in perovskite thickness and crystallization causing difference in luminescence intensity and band gap variation.

Figure 5 gives an example of a spin coated module where a comet-like feature in the perovskite layer is formed around a 100 μ m sized Cl-based dust particle, as shown from EDX. PL peak position map (Figure

2.1 Inhomogeneity classification

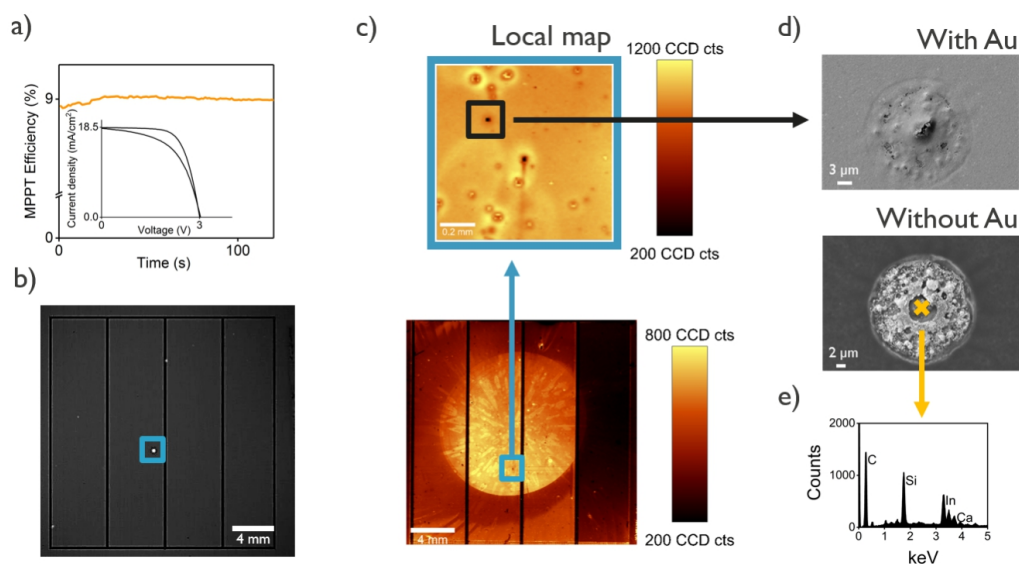


Figure 3: a) MPPT and a hysteresis J-V curve of the module. b) DLIT image at 3.5 V with type 1 inhomogeneity in cell 2. Dark grid indicates where module active area and interconnections are. c) μ PLS intensity map with a high resolution local map. Type 1 inhomogeneity is easily detectable due to sharp drop in PL intensity. d) SEM secondary electron images of the inhomogeneity images with top Au layer and without. e) EDX of the central C-based particle around which the perovskite forms irregularly is presumed to be from PCBM layer underneath.

5b) shows a local variation in perovskite layer bandgap caused by the presence of these inhomogeneities. SEM and EDX are used to identify particles causing these features. As shown in SEM image the lighter areas correspond to the heavier elements in the material, showing that the area directly around the particle lacks or has a very thin layer of perovskite. These nip samples have the perovskite layer covered by a 250 nm thick Spiro-OMeTAD film which fills and evens out such areas to decrease the chances of a metal-oxide shunt formation.

On the other hand, a concentric ring feature around inhomogeneity is visible in the perovskite layer of a blade coated sample as shown in EL and μ PLS peak position (band gap) map in Figure 6a,b. This feature is formed by poor wetting and inadequate perovskite crystallization, represented by the blue layer in FIB cross-section (Figure 6c and Movie provided in SI). Further analysis of these inhomogeneities using μ PLS local mapping, SEM, EDX and FIB shows that they form from dust particles or larger perovskite crystals. Therefore, we hypothesize that type 3 inhomogeneities stem from cleanliness of processing affecting perovskite wetting on underlying layer and non-optimized colloidal precursor perovskite solution. It has been shown that characteristics of precursor solution (choice of solvent, aging, etc.) are crucial factors affecting perovskite crystallization, film morphology and hence device performance. [53;54;55].

2.1 Inhomogeneity classification

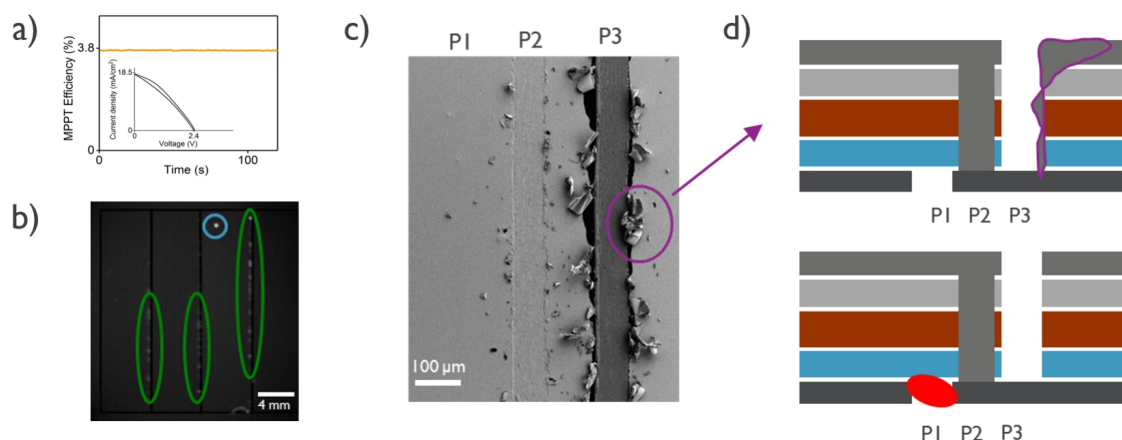


Figure 4: a) MPPT and a J-V curve of the imaged module. b) DLIT image at 3.0 V with type 1 (blue) and 2 (green) inhomogeneities visible. Dark grid indicates where module active area and interconnections are. c) SEM image of mechanically patterned interconnections indicating accumulation of Au material at the P3 interconnection. d) Schemes of module interconnections with a conductive particle located in P1 isolation line or material accumulates at P3, creating a short path for current. Schemes are not drawn to scale since interconnections line have a contact length of 50 - 100 μm , while perovskite module stack is only 1 μm thick.

While these inhomogeneities impede achieving optimal perovskite layer and can affect all parameters of the device, they do not have detrimental effect on short term performance with the studied device stack. However, type 3 inhomogeneities with sizes of 10 - 500 μm can cause cracking in the relatively thin stack of 1 μm (Figure 6c) and might cause longer term degradation.

2.1.4 Type 4

Type 4 represent any inhomogeneity features that result in inactive cell in a pristine module. The studied modules have four cells connected in series, where an inactive cell is easily identified from JV measurements as lack of approximately 1 V in V_{OC} (Figure 3a) and in EL as cell with no luminescence response. Perovskite bandgap map using μPLS show no difference between active and inactive cell perovskite. However, in the μPLS intensity map of these modules, the inactive cell shows lower radiative recombination in comparison to active cells (rightmost cell in a module in Figure 3c). We find that this is also the case with the cells disconnected due to type 2 inhomogeneity, but not for cells that become inactive during characterization due to type 1 inhomogeneity. Previous studies show that I-V measurements can affect luminescence response of perovskite layer due to ion movement.^[39] Therefore, lower PL intensity of these cells is expected to be due to lack of voltage bias across these cells during previous characterization measurements, J-V sweeps, EL and DLIT. We postulate that these cells are inactive due to interconnection faults caused by mechanical

2.1 Inhomogeneity classification

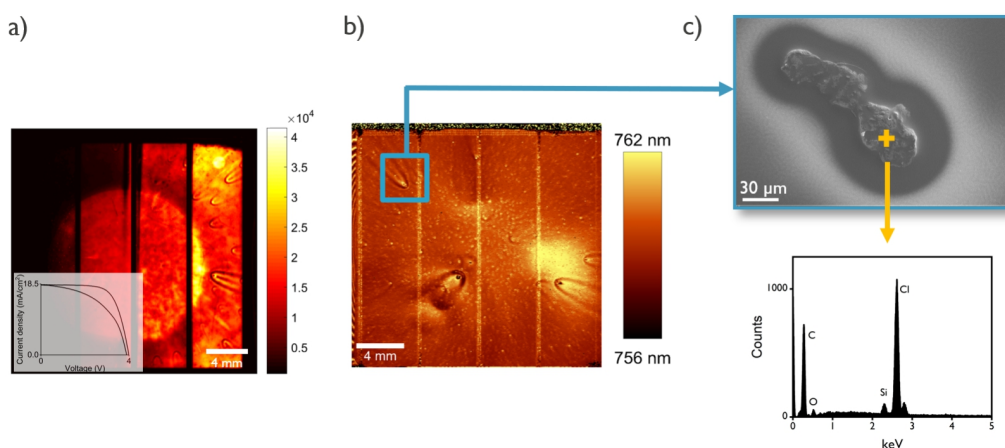


Figure 5: a) EL intensity of a spin coated module after 30 minutes at 4.5 V bias. Inset is a J-V hysteresis measurement of the imaged module. b) μ PLS peak position module map, where type 3 inhomogeneities are even more visible than with EL. c) SEM secondary electron image showing the inhomogeneity causing comet like feature indicated in b. EDX spot measured with 10 KeV indicating carbon signal from HTL layer and Cl from underlying particle.

patterning and therefore disconnected from module circuit. These inhomogeneities can be eliminated by improved mechanical patterning or laser ablation^[31].

2.1.5 Type 5

Inhomogeneities classified as type 5 represent mm size areas that can span across multiple cells in a module. They are detected from variation in luminescence properties in both EL images and μ PLS intensity or band gap maps, pointing to the variation in radiative recombination of perovskite layer. The example of such an inhomogeneity in spin coated modules is a bright circle spanning multiple cells visible in Figure 3c and 5a, while in blade coated samples it can be a gradient in band gap across sample in the blade coating direction as shown by Mundt *et al.*^[36] For spin coated samples, as in Figure 3c and S5 circular bright luminescence area is due to perovskite precursor solution dissolving underlying PCBM solution processed layer. As confirmed by SEM cross-sectional view the area with brighter EL has the same grain size and thickness of perovskite but lack of a PCBM layer, while the darker EL areas had a visible PCBM layer (Figure S5). Therefore, we postulate that in the bright luminescence area, PCBM gets integrated into the perovskite close to interface passivating surface defects^[56], hence decreasing non-radiative recombination in this area. This is further supported by μ PLS maps of spin coated modules where the brighter circles are visible in PL intensity but not on the band gap map, indicating no significant variation of the perovskite layer. Therefore, the appearance of these inhomogeneities indicates the need for optimization of the process for the specific deposition method.

2.2 Spin vs blade coated modules

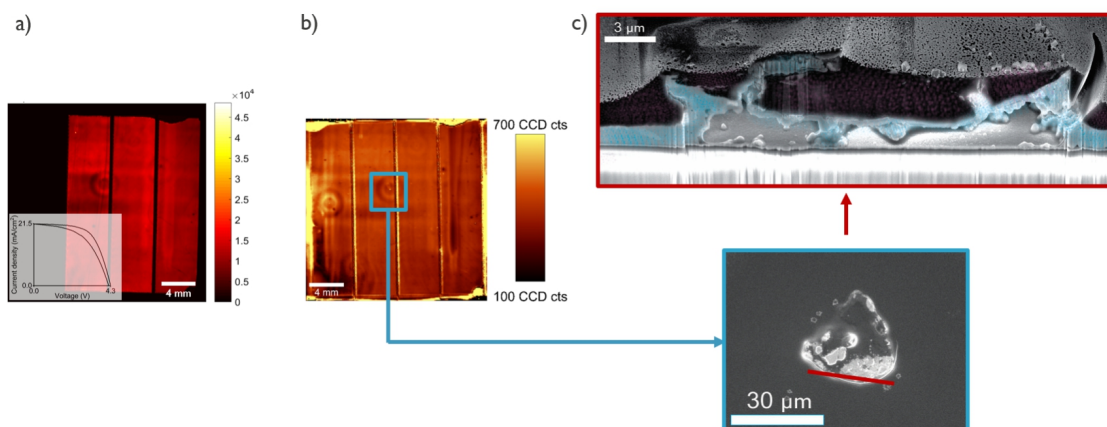


Figure 6: a) EL intensity of a blade coated module after 30 minutes at 4.5 V bias. Inset is a J-V curve of the imaged module. b) μ PLS intensity module map, where type 3 inhomogeneities are visible. c) SEM secondary electron image showing the inhomogeneity causing circular feature indicated in b. d) Red cross section view of the inhomogeneity using FIB where wetting problems of the perovskite on ETL are visible.

2.2 Spin vs blade coated modules

We compare upscaling losses moving from 0.13 cm^2 cell to 4 cm^2 module for spin and blade coated modules. Based on the experimental results and SPICE based simulation[†] we analyze the share of each of the upscaling losses and the effect of the above classified inhomogeneities on total module inhomogeneity loss. J-V measurements of all spin and blade coated modules are given in Figure S4. Higher J_{SC} and V_{OC} of blade coated modules indicate a more homogeneous perovskite layer and stack formation.

The four loss mechanisms in upscaling from cell to module have been defined above (Figure 1a). Figure 7a shows the average upscaling loss split into four specific losses for each deposition method, where total upscaling loss for the spin coated devices equals to $20\%_{rel}$ in comparison to $11\%_{rel}$ for the blade coated devices. While neither of the modules have minimized dead area with a loss of $7-8\%_{rel}$, the main difference in losses comes from the layer inhomogeneity loss. The inhomogeneity loss accounts for $11\%_{rel}$ for spin coated devices in comparison to only $1\%_{rel}$ for blade coated devices. However, even though spin coating devices have higher total upscaling loss, average absolute efficiency for spin coated cells and modules is higher than for blade coated devices.

For an accurate comparison we analyze the reproducibility of the device performance for each of the deposition methods, as seen in Figure 7b. Each module performance is compared to the best cell performance, where spin coated modules always under-perform cell devices and show reproducible performance among substrates. On the other hand, blade coated devices have low reproducibility, while 50% of the processed

2.2 Spin vs blade coated modules

module devices have equal or higher performance than the reference cell. Keeping in mind that both small area cell devices and module devices are processed on equal size (9 cm^2) substrates, comparable performance of cell and module devices indicates that indeed blade coating provides more homogeneous layers over the whole substrate. However, larger variation in performance among blade coated modules and lower absolute performance of blade coated cells and modules indicates a need for further optimization of the blade coating process.

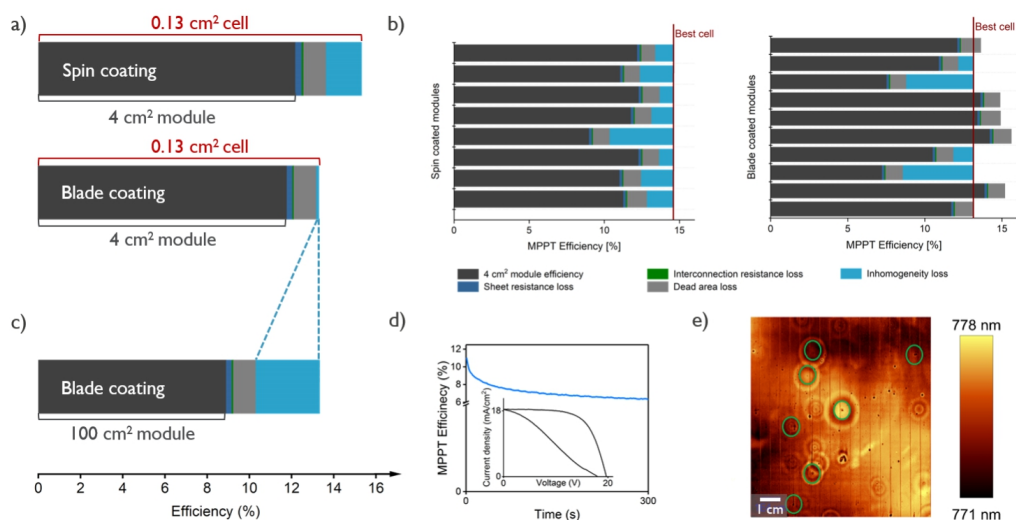


Figure 7: a) Stack diagram showing difference in PCE between best 0.13 cm^2 cell and average 4 cm^2 module with different colors representing the four upscaling losses in $\%_{abs}$. b) Comparison of efficiency of the best 0.13 cm^2 cell to each of the 4 cm^2 modules for spin and blade coated modules, indicating a share of each of the four upscaling losses. c) Stack diagram showing difference in PCE between 0.13 cm^2 cell and 100 cm^2 module with different colors representing the four upscaling losses in $\%_{abs}$. d) J-V hysteresis and MPPT measurement of 100 cm^2 module. and e) μ PLS peak position map showing 18 out of 20 serially connected cells in a 100 cm^2 module with few type 3 inhomogeneities circled with green color.

Since the inhomogeneity loss is the most pronounced when upscaling, it is analyzed based on the above defined inhomogeneity types. Type 2, 4 and 5 inhomogeneities are detected only in spin coated modules. The type 5 loss is closely related to the process of the used deposition method. Therefore, type 5 inhomogeneity could be avoided with spin coated samples with optimized spin coating process where dynamic instead of static spin coating of perovskite layer^[57] is used, minimizing a dissolution of the underlying PCBM layer. Type 2 and 4 inhomogeneities are formed due to interconnections and affect the module performance through a decrease in V_{OC} (Figure S4) for 20 % of the spin coated samples. These inhomogeneities are not present in the blade coated module due to two factors: slight improvement in mechanical patterning process due to change in the blade used for patterning in between the batch processing and lower number of particles

2.2 Spin vs blade coated modules

visible on blade coated samples, lowering the risk of particles being localized at the interconnection lines. Type 1 and 3 inhomogeneities are present in both types of samples, where type 3 inhomogeneities are more pronounced in spin coated devices and type 1 in blade coated devices. High density of type 3 inhomogeneities is visible in EL images and μ PLS maps of spin coated modules (Figure 5 versus Figure 6). An increased number of type 3 inhomogeneities in spin coated modules could be the explanation for lower V_{OC} that reaches 4 V (1 V per cell) for spin coated and 4.3 V (1.07 V per cell) for blade coated modules (Figure S4). On the other hand, type 1 inhomogeneities are more common in blade coated samples, which is due to pinholes in processed perovskite layer caused by cleanliness of the processing atmosphere or the processing method. The chosen processing method includes a deposition of the precursor solution followed by the formation of an intermediate perovskite phase which is completely crystallized upon thermal treatment. We postulate that improvement in wetting of the underlying layer and avoiding the pinholes in the perovskite layer could be achieved using process with direct crystallization or by improvements in solvent engineering of deposited ink. [4;9;14;58]

If modules affected by type 1, 2 and 4 inhomogeneities are excluded, the spin coated modules have average inhomogeneity loss of 8.8 %_{rel} due to type 3 and 5 inhomogeneities. Moreover, assuming decrease in J_{SC} of spin coated modules in comparison to spin coated small area cells (Figure S4) is only due to inactive area loss and current mismatch among cells due to type 5 inhomogeneities, module loss due to type 3 inhomogeneities would be responsible for 5.2 %_{rel} loss in going from cell to module or 50 % of the total inhomogeneity loss. Therefore, progress in solvent engineering and control of perovskite crystallization as processing strategy that would decrease type 3 inhomogeneity would have crucial effect on decrease of the layer inhomogeneity loss.

In Figure 7b, the module performance is compared to the best cell by adding interconnection resistance, inactive area and sheet resistance losses which are unavoidable based on the interconnection process and module design. When these losses are accounted for, 60 % of blade coated modules achieve or surpass the performance of the best cell. Therefore, in the remaining 40 % of modules the dominant inhomogeneity loss is attributed to type 1 and 3 losses. The lack of dark IV measurements for these devices prevents us from quantifying the impact of these two inhomogeneity loss types separately.

Based on the comparison of average performance of 4 cm² devices (Figure 7a), linear deposition method promises a minimized layer inhomogeneity loss. However, further increase in substrate size from 9 to 125 cm² using linear deposition method brings focus back on inhomogeneity loss, as the largest loss mech-

anism. This is evident from a lower efficiency with 100 cm² aperture area module, owing to a 20%_{rel} inhomogeneity loss (Figure 7c). Large area, modules of 100 cm² were not encapsulated and therefore during characterization steps samples were exposed to ambient air at room temperature (Figure 7e and S6). Our characterization process detects type 1, 3 and 5 inhomogeneities (Figure S6). The presence of type 5 inhomogeneity, visible in μ PLS band gap map (Figure 7e), indicates non-uniform perovskite crystallization across the large substrate and a need for optimization of the process. Moreover, a significant increase in type 3 inhomogeneities is visible as, even up to, millimeter sized lines and concentric rings around inhomogeneity source, detected by μ PL intensity and band gap maps (Figure 7e and S6). An impact of type 3 inhomogeneities is reflected in a V_{OC} per cell of 1 V in comparison to 1.08 V with 4 cm² modules (Figure 7d). Therefore, even though linear coating techniques offer a better control and uniformity of crystallization as seen with 4 cm² devices, a careful control of the processing conditions, substrate pre-perovskite treatment and solvent engineering become even more critical for further upscaling.

3 Conclusions

This study shows that dark lock-in thermography and luminescence imaging are valuable tools to define pitfalls and areas for further improvements of perovskite module processing. Upscaling from cell to module introduces multiple loss mechanisms. The layer inhomogeneity loss is the main loss mechanism since it can scale with device size, hindering successful processing of highly efficient large area perovskite devices. Therefore, understanding the causes of the inhomogeneity loss for different deposition methods is crucial. We applied characterization process including luminescence imaging, thermography and electron microscopy on solution processed perovskite devices with aperture area up to 100 cm² to analyze and identify different types of inhomogeneities and their sources .

We identified three main strategies to overcome pitfalls in current upscaling practices that are responsible for layer inhomogeneities: cleaner processing, more efficient module interconnection patterning and a better understanding and control of all phases of the multi-cation perovskite crystallization process. Cleaner processing pertains to the processing environment, substrate treatment and controlled solutions. While this is a main pitfall of research laboratories it is easy to control in industrial processing. Interconnection patterning using laser processing is already in use and being optimized by many labs using ps or ns pulsed lasers. The last but crucial factor in an effective upscaling is understanding and control of the perovskite crystallization process. Even though multiple studies have analyzed the crystallization of CH₃NH₃PbI₃ perovskite

REFERENCES

processed with various deposition techniques, where a defined temperature, the precursor solution, the interaction between precursors and solvents, the interaction between precursor and substrate, the processing atmosphere, purity of chemicals and interfacial strain are the most important factors affecting quality of crystallized perovskite semiconductor, the interplay of these effects on nucleation and growth are still not clear^[4]. Moreover, crystalization dynamics of multi-cation perovskite compositions as used in this study are still unknown.

While the knowledge on perovskite crystallization can be acquired from spin coating techniques, a transfer from spin coating to other upscalable methods is not direct and therefore the community should strongly focus on matching achieved small area performance with upscalable deposition methods. While the current progress in performance of upscaled devices is encouraging, this study emphasizes the need for systematic approach to processing of upscaled devices.

Supporting information

Supporting Information is available from the Wiley Online Library or from the author.

Acknowledgments

Authors would like to thank Jutta Zielonka for her work on SEM/EDX/FIB imaging of perovskite modules. Lucija Rakocevic was funded by Research Foundation - Flanders (FWO) for doctoral student research visit. This project has received funding from the European Union's H2020 Programme for research, technological development and demonstration under grant agreement no. 764047 of the ESPReso project.

Conflict of interest

There are no conflicts to declare.

References

- [1] L. K. Ono, Y. Qi, *J. Phys. D: Appl. Phys.* 2018, 51, 093001.
- [2] F. Huang, M. Li, P. Siffalovic, G. Cao, J. Tian, *Energy Environ. Sci.* 2019, 12, 518.

REFERENCES

- [3] A. K. Jena, A. Kulkarni, T. Miyasaka, *Chem. Rev.* 2019, 119, 3036.
- [4] W. A. Dunlap-Shohl, Y. Zhou, N. P. Padture, D. B. Mitzi, *Chem. Rev.* 2019, 119, 3193.
- [5] D. Pérez-del-Rey, P. P. Boix, M. Sessolo, A. Hadipour, H. J. Bolink, *J. Phys. Chem. Lett.* 2018, 9, 1041.
- [6] F. Mathies, H. Eggers, B. S. Richards, G. Hernandez-Sosa, U. Lemmer, U. W. Paetzold, *ACS Appl. Energy Mater.* 2018, 1, 1834.
- [7] W. Qiu, T. Merckx, M. Jaysankar, C. M. de la Huerta, L. Rakocevic, W. Zhang, U. W. Paetzold, R. Gehlhaar, L. Froyen, J. Poortmans, D. Cheyns, H. J. Snaith, P. Heremans, *Energy Environ. Sci.* 2016, 9, 484.
- [8] J. G. Tait, S. Manghooli, W. Qiu, L. Rakocevic, L. Kootstra, M. Jaysankar, C. A. M. de la Huerta, U. W. Paetzold, R. Gehlhaar, D. Cheyns, P. Heremans, J. Poortmans, *J. Mater. Chem. A* 2016, 4, 3792.
- [9] F. Ye, W. Tang, F. Xie, M. Yin, J. He, Y. Wang, H. Chen, Y. Qiang, X. Yang, L. Han, *Adv. Mater. Weinheim* 2017, 29, DOI 10.1002/adma.201701440.
- [10] Z. Song, C. L. McElvany, A. B. Phillips, I. Celik, P. W. Krantz, S. C. Wathage, G. K. Liyanage, D. Apul, M. J. Heben, *Energy Environ. Sci.* 2017, 10, 1297.
- [11] F. A. Roghabadi, M. Alidaei, S. M. Mousavi, T. Ashjari, A. S. Tehrani, V. Ahmadi, S. M. Sadrameli, *J. Mater. Chem. A* 2019, 7, 5898.
- [12] H. Higuchi, T. Negami, *Jpn. J. Appl. Phys.* 2018, 57, 08RE11.
- [13] F. Di Giacomo, S. Shanmugam, H. Fledderus, B. J. Bruijnaers, W. J. H. Verhees, M. S. Dorenkamper, S. C. Veenstra, W. Qiu, Gehlhaar, T. Merckx, T. Aernouts, R. Andriessen, Y. Galagan, *Solar Energy Materials and Solar Cells* 2018, 181, 53.
- [14] Z. Yang, S. Zhang, L. Li, W. Chen, *Journal of Materiomics* 2017, 3, 231.
- [15] M. Yang, D. H. Kim, T. R. Klein, Z. Li, M. O. Reese, B. J. Tremolet de Villers, J. J. Berry, M. F. A. M. van Hest, K. Zhu, *ACS Energy Lett.* 2018, 3, 322.
- [16] S. Hong, J. Lee, H. Kang, G. Kim, S. Kee, J.-H. Lee, S. Jung, B. Park, S. Kim, H. Back, K. Yu, K. Lee, *Science Advances* 2018, 4, eaat3604.

REFERENCES

- [17] E. Calabro, F. Matteocci, A. L. Palma, L. Vesce, B. Taheri, L. Carlini, I. Pis, S. Nappini, J. Dagar, C. Battocchio, T. M. Brown, A. Di Carlo, *Solar Energy Materials and Solar Cells* 2018, 185, 136.
- [18] Y. Deng, X. Zheng, Y. Bai, Q. Wang, J. Zhao, J. Huang, *Nature Energy* 2018, 3, 560.
- [19] Y. Rong, Y. Ming, W. Ji, D. Li, A. Mei, Y. Hu, H. Han, *J. Phys. Chem. Lett.* 2018, 9, 2707.
- [20] J. Li, R. Munir, Y. Fan, T. Niu, Y. Liu, Y. Zhong, Z. Yang, Y. Tian, B. Liu, J. Sun, D. M. Smilgies, S. Thoroddsen, A. Amassian, K. Zhao, S. (Frank) Liu, *Joule* 2018, 2, 1313.
- [21] Y. Galagan, F. D. Giacomo, H. Gortler, G. Kirchner, I. de Vries, R. Andriessen, P. Groen, *Advanced Energy Materials* 2018, 8, 1801935.
- [22] J.-W. Lee, D.-K. Lee, D.-N. Jeong, N.-G. Park, *Advanced Functional Materials* 2018, 0, 1807047.
- [23] Y. Rong, Y. Hu, A. Mei, H. Tan, M. I. Saidaminov, S. I. Seok, M. D. McGehee, E. H. Sargent, H. Han, *Science* 2018, 361, eaat8235.
- [24] “Best Research-Cell Efficiency Chart | Photovoltaic Research | NREL,” can be found under <https://www.nrel.gov/pv/cell-efficiency.html>, Accessed June 21st 2019.
- [25] B. Wilkinson, N. L. Chang, M. A. Green, A. W. Y. Ho-Baillie, *Progress in Photovoltaics: Research and Applications* 2018, 26, 659.
- [26] J. Kim, J. S. Yun, Y. Cho, D. S. Lee, B. Wilkinson, A. M. Soufiani, X. Deng, J. Zheng, A. Shi, S. Lim, S. Chen, Z. Hameiri, M. Zhang, C. F. J. Lau, S. Huang, M. A. Green, A. W. Y. Ho-Baillie, *ACS Energy Lett.* 2017, 2, 1978.
- [27] H. Hoppe, M. Seeland, B. Muhsin, *Solar Energy Materials and Solar Cells* 2012, 97, 119.
- [28] S. Moon, J. Yum, L. Lofgren, A. Walter, L. Sansonnens, M. Benkhaira, S. Nicolay, J. Bailat, C. Ballif, *IEEE Journal of Photovoltaics* 2015, 5, 1087.
- [29] S. Razza, S. Castro-Hermosa, A. Di Carlo, T. M. Brown, *APL Materials* 2016, 4, 091508.
- [30] L. Gao, L. Chen, S. Huang, X. Li, G. Yang, *ACS Appl. Energy Mater.* 2019, DOI 10.1021/acsaem.9b00531.
- [31] L. Rakocevic, R. Gehlhaar, T. Merckx, W. Qiu, U. W. Paetzold, H. Fledderus, J. Poortmans, *IEEE Journal of Photovoltaics* 2017, 7, 404.

REFERENCES

- [32] T. W. Jones, A. Osherov, M. Alsari, M. Sponseller, B. C. Duck, Y.-K. Jung, C. Settens, F. Niroui, R. Brenes, C. V. Stan, Y. Li, M. Abdi-Jalebi, N. Tamura, J. E. Macdonald, M. Burghammer, R. H. Friend, V. Bulović, A. Walsh, G. J. Wilson, S. Lilliu, S. D. Stranks, *Energy Environ. Sci.* 2019, 12, 596.
- [33] S. Mastroianni, F. D. Heinz, J.-H. Im, W. Veurman, M. Padilla, M. C. Schubert, U. Würfel, M. Grätzel, N.-G. Park, A. Hinsch, *Nanoscale* 2015, 7, 19653.
- [34] D. W. deQuilettes, W. Zhang, V. M. Burlakov, D. J. Graham, T. Leijtens, A. Osherov, V. Bulović, H. J. Snaith, D. S. Ginger, S. D. Stranks, *Nature Communications* 2016, 7, 11683.
- [35] Z. Hameiri, A. M. Soufiani, M. K. Juhl, L. Jiang, F. Huang, Y.-B. Cheng, H. Kampwerth, J. W. Weber, M. A. Green, T. Trupke, *Progress in Photovoltaics: Research and Applications* 2015, 23, 1697.
- [36] L. E. Mundt, W. Kwapil, M. A. Yakoob, J. P. Herterich, M. Kohlstädt, U. Würfel, M. C. Schubert, S. W. Glunz, *IEEE Journal of Photovoltaics* 2019, 9, 452.
- [37] B. Chen, J. Peng, H. Shen, T. Duong, D. Walter, S. Johnston, M. M. Al-Jassim, K. J. Weber, T. P. White, K. R. Catchpole, D. Macdonald, H. T. Nguyen, *Advanced Energy Materials* 2018, 9, 1802790.
- [38] G. El-Hajje, C. Momblona, L. Gil-Escrig, J. Avila, T. Guillemot, J.-F. Guillemoles, M. Sessolo, H. J. Bolink, L. Lombez, *Energy Environ. Sci.* 2016, 9, 2286.
- [39] A. M. Soufiani, Z. Hameiri, S. Meyer, S. Lim, M. J. Y. Tayebjee, J. S. Yun, A. Ho-Baillie, G. J. Conibeer, L. Spiccia, M. A. Green, *Advanced Energy Materials* 2017, 7, 1602111.
- [40] A. M. Soufiani, J. Kim, A. Ho-Baillie, M. Green, Z. Hameiri, *Advanced Energy Materials* 2018, 8, 1702256.
- [41] W. Qiu, J. P. Bastos, S. Dasgupta, T. Merckx, I. Cardinaletti, M. V. C. Jenart, C. B. Nielsen, R. Gehlhaar, J. Poortmans, P. Heremans, I. McCulloch, D. Cheyns, *J. Mater. Chem. A* 2017, 5, 2466.
- [42] M. Saliba, T. Matsui, J.-Y. Seo, K. Domanski, J.-P. Correa-Baena, M. K. Nazeeruddin, S. M. Zakeeruddin, W. Tress, A. Abate, A. Hagfeldt, M. Grätzel, *Energy Environ. Sci.* 2016, 9, 1989.
- [43] L. Rakocevic, F. Ernst, N. T. Yimga, S. Vashishtha, T. Aernouts, T. Heumueller, C. J. Brabec, R. Gehlhaar, J. Poortmans, *Solar RRL* 2019, 3, 1800287.

REFERENCES

- [44] P. Gundel, F. D. Heinz, M. C. Schubert, J. A. Giesecke, W. Warta, *Journal of Applied Physics* 2010, 108, 033705.
- [45] M. Okano, M. Endo, A. Wakamiya, M. Yoshita, H. Akiyama, Y. Kanemitsu, *Appl. Phys. Express* 2015, 8, 102302.
- [46] A. Walter, S. Moon, B. A. Kamino, L. Lofgren, D. Sacchetto, F. Matteocci, B. Taheri, J. Bailat, A. D. Carlo, C. Ballif, S. Nicolay, *IEEE Journal of Photovoltaics* 2018, 8, 151.
- [47] Y. Wu, H. Shen, D. Walter, D. Jacobs, T. Duong, J. Peng, L. Jiang, Y.-B. Cheng, K. Weber, *Advanced Functional Materials* 2016, 26, 6807.
- [48] A. R. Bowering, L. Bertoluzzi, B. C. O'Regan, M. D. McGehee, *Advanced Energy Materials* 2018, 8, 1702365.
- [49] P. Vorasayan, T. R. Betts, A. N. Tiwari, R. Gottschalg, *Solar Energy Materials and Solar Cells* 2009, 93, 917.
- [50] Z. Song, J. Werner, N. Shrestha, F. Sahli, S. De Wolf, B. Niesen, S. C. Watthage, A. B. Phillips, C. Ballif, R. J. Ellingson, M. J. Heben, *J. Phys. Chem. Lett.* 2016, 7, 5114.
- [51] L. Bayer, X. Ye, P. Lorenz, K. Zimmer, *Appl. Phys. A* 2017, 123, 619.
- [52] L. Rakocevic, R. Gehlhaar, M. Jaysankar, W. Song, T. Aernouts, H. Fledderus, J. Poortmans, *J. Mater. Chem. C* 2018, 6, 3034.
- [53] Y. Zhou, O. S. Game, S. Pang, N. P. Padture, *J. Phys. Chem. Lett.* 2015, 6, 4827.
- [54] K. Yan, M. Long, T. Zhang, Z. Wei, H. Chen, S. Yang, J. Xu, *J. Am. Chem. Soc.* 2015, 137, 4460.
- [55] M. Jung, S.-G. Ji, G. Kim, S. I. Seok, *Chem. Soc. Rev.* 2019, 48, 2011.
- [56] L. Zhou, J. Chang, Z. Liu, X. Sun, Z. Lin, D. Chen, C. Zhang, J. Zhang, Y. Hao, *Nanoscale* 2018, 10, 3053.
- [57] F. Yang, D.-W. Kang, Y.-S. Kim, *RSC Adv.* 2017, 7, 19030.
- [58] M. K. Kim, H. S. Lee, S. R. Pae, D.-J. Kim, J.-Y. Lee, I. Gereige, S. Park, B. Shin, *J. Mater. Chem. A* 2018, 6, 24911.